

On-chip control of the coherence matrix of four-mode partially coherent light: rank, entropy, and modal Stokes parameters

Amin Hashemi,¹ Abbas Shiri,¹ Bahaa E. A. Saleh,¹ Andrea Blanco-Redondo,¹ and Ayman F. Abouraddy¹

¹*CREOL, The College of Optics & Photonics, University of Central Florida, Orlando, FL 32816, USA*

Partially coherent light offers salutary capabilities in optical information processing that cannot be matched by coherent light. To date, this ‘coherence advantage’ has been confirmed in proof-of-principle optical communications protocols using bulk optics. Taking full advantage of such opportunities necessitates processing multimode partially coherent light in integrated photonics platforms that alone provide the requisite stability for cascaded operations on a large scale. Here we demonstrate on-chip manipulation of four-mode partially coherent light described by a 4×4 Hermitian coherence matrix. Starting with generic maximally incoherent light, we utilize an on-chip hexagonal mesh of Mach-Zehnder interferometers to perform all the unitary and non-unitary tasks that are critical for realizing structured coherence: controlling the coherence rank (the number of non-zero eigenvalues of the coherence matrix); tuning the field entropy; molding the structure of the coherence matrix via 4×4 unitary transformations constructed out of sequences of 2×2 unitaries acting on pairs of modes; and tomographic reconstruction of the coherence matrix by measuring the modal Stokes parameters associated with Kronecker Pauli matrices. These results confirm the scalability of utilizing 2×2 on-chip building blocks for the synthesis and reconstruction of high-dimensional coherence matrices, and provide a decisive step towards large-scale on-chip manipulation of massively moded partially coherent light for applications in optical information processing.

I. INTRODUCTION

Because all natural sources of light – from solar and stellar radiation to fluorescence and luminescence – are partially coherent, the study of optical coherence has long been pursued [1–3] and is now a well-established branch of optical physics [4]. Since its inception [5–9], the spatiotemporal dynamics of partially coherent light has been described within a framework of continuous correlation functions (in addition to polarization) [10, 11], with applications extending from propagation in turbulent media [12–14], to sensing and metrology [15, 16]. However, recent findings making use of a discrete formulation of optical coherence have unveiled a ‘coherence advantage’ in optical information processing, wherein partially coherent light outperforms its coherent counterpart [17–19]. One example occurs in communicating optically across a channel supporting N modes (such as a multimode fiber or a bundle of single-mode fibers), where coherent light supports $\mathcal{O}(N)$ independent communications signals, whereas partially coherent light supports $\mathcal{O}(N^2)$ [17]. In another example, the coherence rank (the number of non-zero eigenvalues of the coherence matrix) was exploited as a scattering-immune information carrier – even when the scattering is strong (arbitrary modal coupling) and the channel characteristics change from bit to bit (thus precluding the use of adaptive optics) [19].

These applications, along with other recent results [18, 20], motivate the transition from free-space optics – which remains to date the exclusive domain for the experimental investigation of partially coherent light – to integrated-photonics platforms for the manipulation of spatial coherence in massive arrays of single-mode waveguides. Such platforms [21–24] alone offer the requisite conditions for versatile exploitation of the ‘coher-

ence advantage’ in optical information processing: small footprints that enable scaling up the number of optical modes, high-speed processing, and the interferometric stability needed for large-scale cascading of optical transformations. Substantial progress has been made in on-chip processing of quantum and classical optical fields, which has nevertheless focused on pure states in the former and coherent light in the latter. It remains now for these advances to be harnessed for the processing of partially coherent light. On-chip manipulation of two-mode partially coherent optical fields has been recently demonstrated, including molding the two-mode coherence matrix via 2×2 unitary transformations (‘unitaries’ henceforth for brevity), which are the building blocks for larger-dimensional unitaries [22, 25–27].

Here we demonstrate for the first time scalable on-chip loading, unitary and non-unitary manipulation, and reconstruction of partial coherence in the spatial domain, realized here using four-mode partially coherent optical fields. The integrated-photonics platform utilized here comprises a large hexagonal array of programmable Mach-Zehnder interferometers (MZIs). We first produce a generic four-mode mutually incoherent spatial field in single-mode fibers starting from a short-coherence-length laser diode with that can be efficiently coupled to on-chip single-mode waveguides. Second we control the coherence rank of the field by selectively eliminating on chip the modal weights (a non-unitary linear operation), from rank-1 fields (fully coherent light extracted from the initial generic incoherent light) to maximally incoherent rank-4 fields. Third, we tune the entropy of the field without changing the rank, another non-unitary linear operations. We further synthesize iso-entropy rank-3 and rank-4 optical fields that cannot be inter-converted unitarily [28]. Fourth, we construct examples of on-chip 4×4

unitaries that modify the structure of the coherence matrix, thereby enabling control over the real and imaginary parts of its off-diagonal elements. Fifth, we reconstruct the coherence matrix by measuring the modal Stokes parameters mediated by Kronecker 4×4 Pauli matrices formed of direct products of the usual 2×2 Pauli matrices. These results demonstrate that on-chip platforms are capable of performing all the critical tasks needed for the reliable processing of massively multimoded partially coherent light, which is expected to enable new fundamental studies of partial coherence [29–31] and utilizing such optical fields in communications, cryptography, spectroscopy, sensing and metrology, and computation.

II. COHERENCE MATRIX FOR A FOUR-MODE FIELD

We consider an optical field spanned by four modes labeled $\{|1\rangle, |2\rangle, |3\rangle, |4\rangle\}$ in the Dirac notation, which correspond to the fields in four single-mode on-chip waveguides. A coherent field in this basis is described by the vector $|E\rangle = \sum_{j=1}^4 E_j |j\rangle$, and the normalization $\langle E|E\rangle = 1$ entails that $\sum_{j=1}^4 |E_j|^2 = 1$. We refer to the squared magnitude $|E_j|^2$ as the modal weight, which is the fraction of power associated with the j^{th} -mode. A partially coherent field is described by the 4×4 coherence matrix [30, 32–35]:

$$\mathbf{G} = \begin{pmatrix} G_{11} & G_{12} & G_{13} & G_{14} \\ G_{21} & G_{22} & G_{23} & G_{24} \\ G_{31} & G_{32} & G_{33} & G_{34} \\ G_{41} & G_{42} & G_{43} & G_{44} \end{pmatrix}, \quad (1)$$

where $G_{jk} = \langle E_j E_k^* \rangle$, $j, k = 1, 2, 3, 4$, and $\langle \cdot \rangle$ is a statistical average over an ensemble. The coherence matrix is Hermitian $\mathbf{G}^\dagger = \mathbf{G}$, so that $G_{jk} = G_{kj}^*$, and \mathbf{G} is normalized so that $\text{Tr}\{\mathbf{G}\} = 1$, where $\text{Tr}\{\cdot\}$ refers to the matrix trace. The diagonal elements G_{jj} are the modal weights, and the off-diagonal element G_{jk} , $j \neq k$, determines the interference visibility resulting from superposing the j^{th} and k^{th} modes.

The Hermitian coherence matrix \mathbf{G} can be diagonalized via a 4×4 unitary \hat{U} such that $\hat{U} \mathbf{G} \hat{U}^\dagger = \mathbf{G}^D$, where \mathbf{G}^D is a diagonal coherence matrix,

$$\mathbf{G}^D = \begin{pmatrix} \lambda_1 & 0 & 0 & 0 \\ 0 & \lambda_2 & 0 & 0 \\ 0 & 0 & \lambda_3 & 0 \\ 0 & 0 & 0 & \lambda_4 \end{pmatrix} = \text{diag}\{\lambda_1, \lambda_2, \lambda_3, \lambda_4\}, \quad (2)$$

$\lambda_1, \lambda_2, \lambda_3$, and λ_4 are the eigenvalues of \mathbf{G} , $\lambda_j \geq 0$, we arrange the eigenvalues in descending order, $\sum_{j=1}^4 \lambda_j = 1$, and the shorthand $\text{diag}\{\dots\}$ indicates a diagonal matrix with the entries representing the diagonal elements. The entropy of a coherence matrix is given by

$$S = -\text{Tr}\{\mathbf{G} \log_2 \mathbf{G}\} = -\sum_{j=1}^4 \lambda_j \log_2 \lambda_j, \quad (3)$$

with $0 \leq S \leq 2$. A coherence matrix corresponds to a field configuration in which the correlations between all pairs of modes have been eliminated, so that no interference fringes are observed when overlapping any two modes.

We make use of a fourfold classification of partially coherent four-mode fields according to the ‘coherence rank’, which is defined as the number of non-zero eigenvalues of \mathbf{G} [28, 31]. Rank-1 fields ($\lambda_2 = \lambda_3 = \lambda_4 = 0$) are coherent with $S = 0$, corresponding to a complete lack of statistical fluctuations. We take $\mathbf{G}_1 = \text{diag}\{1, 0, 0, 0\}$ as a representative rank-1 coherence matrix. Rank-2 fields ($\lambda_3 = \lambda_4 = 0$) have $0 < S \leq 1$ bit, and we take the maximum-entropy coherence matrix $\mathbf{G}_2 = \text{diag}\{\frac{1}{2}, \frac{1}{2}, 0, 0\}$ ($S = 1$ bit) as representative. Rank-3 fields ($\lambda_4 = 0$) have $0 < S \leq \log_2 3$ bits, and we take the maximum-entropy coherence matrix $\mathbf{G}_3 = \text{diag}\{\frac{1}{3}, \frac{1}{3}, \frac{1}{3}, 0\}$ ($S = \log_2 3 \approx 1.585$ bits) as representative. Finally, all the eigenvalues of rank-4 fields are non-zero, with $0 < S \leq 2$ bits, and we take the maximum-entropy coherence matrix $\mathbf{G}_4 = \text{diag}\{\frac{1}{4}, \frac{1}{4}, \frac{1}{4}, \frac{1}{4}\}$ ($S = 2$ bits) as representative. These four representative coherence matrices, \mathbf{G}_1 through \mathbf{G}_4 , are the basis for the coherence-rank-communications experiment in Ref. [19], and we thus take them as starting points for the unitaries to be implemented here.

III. CONSTRUCTION OF A GENERAL ON-CHIP UNITARY

We make use in our experiments of the hexagonal mesh of 72 MZIs (iPronics Smartlight Processor) depicted in Fig. 1(a). We combine MZIs to construct general 2×2 unitaries operating on two modes at a time, a sequence of which can be assembled into a 4×4 unitary.

A. Two-mode on-chip unitaries

We take the building-block 2×2 unitaries to be in the form:

$$\hat{U}(\delta, \alpha) = ie^{i\varphi} \begin{pmatrix} \sin \frac{\delta}{2} & e^{-i\alpha} \cos \frac{\delta}{2} \\ e^{i\alpha} \cos \frac{\delta}{2} & -\sin \frac{\delta}{2} \end{pmatrix}. \quad (4)$$

Each on-chip MZI is formed of a phase operator $\hat{S}(\varphi_1, \varphi_2) = \begin{pmatrix} e^{i\varphi_1} & 0 \\ 0 & e^{i\varphi_2} \end{pmatrix}$ sandwiched between two symmetrical couplers described by the operator $\hat{B} = \frac{1}{\sqrt{2}} \begin{pmatrix} 1 & i \\ i & 1 \end{pmatrix}$ [Fig. 1(b)]:

$$\hat{U}_{\text{MZI}}(\delta, \varphi) = \hat{B} \hat{S}(\varphi_1, \varphi_2) \hat{B} = ie^{i\varphi} \begin{pmatrix} \sin \frac{\delta}{2} & \cos \frac{\delta}{2} \\ \cos \frac{\delta}{2} & -\sin \frac{\delta}{2} \end{pmatrix}, \quad (5)$$

where $\varphi = \frac{1}{2}(\varphi_1 + \varphi_2)$ and $\delta = \varphi_1 - \varphi_2$. Sandwiching this MZI between phase operators $\hat{S}(\alpha) = \begin{pmatrix} e^{i\alpha/2} & 0 \\ 0 & e^{-i\alpha} \end{pmatrix}$

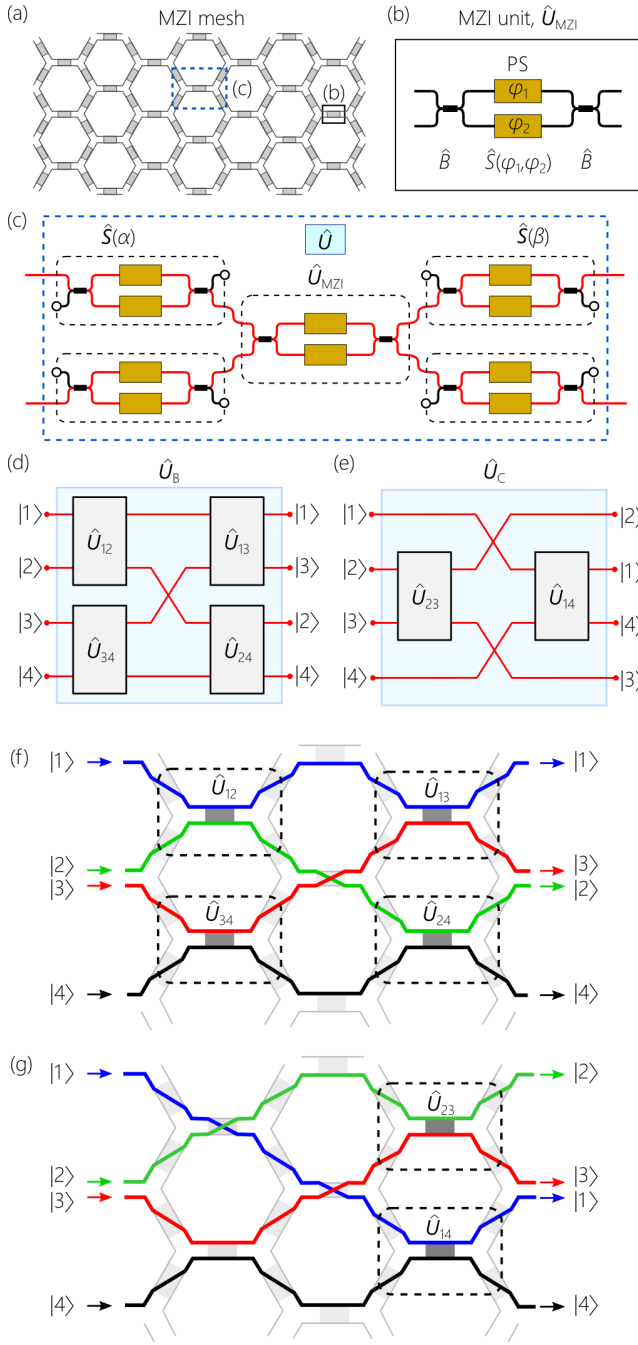


FIG. 1. (a) Chip layout of the MZI mesh. Each colored rectangle is an MZI, and lines are single-mode waveguides. (b) Structure of a single MZI (Eq. 5). PS: Phase shifter. (c) A general 2×2 unitary (Eq. 4) formed of the MZIs highlighted in (a). (d) Construction of the unitary \hat{U}_B and (e) \hat{U}_C out of sequences of 2×2 unitaries. (f) Chip layouts for \hat{U}_B and (g) for \hat{U}_C .

and $\hat{S}(\beta)$ – each implemented in turn by MZIs [Fig. 1(c)] – that introduce phases α and β between the two modes, respectively, yields the general unitary in Eq. 4 after setting $\beta = -\alpha$: $\hat{U}(\delta, \alpha) = \hat{S}(-\alpha)\hat{U}_{\text{MZI}}(\delta, \varphi)\hat{S}(\alpha)$.

B. Four-mode on-chip unitaries

Using such 2×2 unitaries, in addition to phases added to each mode, an arbitrary 4×4 unitary can be constructed as established in mathematics and in quantum information processing [25, 36]. We realize in our experiments here three distinct unitaries. The first is the identity $\hat{U}_A = \hat{\mathbb{I}}_4$, where $\hat{\mathbb{I}}_4$ is the 4×4 identity matrix, which allows us to validate the process of coherence-matrix reconstruction as outlined in the next Section. The other unitaries we construct, \hat{U}_B and \hat{U}_C , are illustrated schematically in Fig. 1(d,e), where:

$$\hat{U}_B = \frac{1}{2} \begin{pmatrix} 1 & 1 & -i & i \\ 1 & -1 & -i & -i \\ i & i & -1 & 1 \\ -i & i & 1 & 1 \end{pmatrix},$$

$$\hat{U}_C = \frac{1}{2} \begin{pmatrix} 1 & 0 & 0 & \sqrt{3}e^{-i\pi/3} \\ 0 & \sqrt{3} & e^{-i\pi/6} & 0 \\ 0 & e^{i\pi/6} & -\sqrt{3} & 0 \\ \sqrt{3}e^{i\pi/3} & 0 & 0 & -1 \end{pmatrix}. \quad (6)$$

These two unitaries are constructed from the 2×2 unitary building blocks [Fig. 1(c)], each operating on the pair of modes identified by their indices, given by:

$$\hat{U}_{12} = \frac{1}{\sqrt{2}} \begin{pmatrix} 1 & 1 \\ 1 & -1 \end{pmatrix}, \quad U_{34} = \frac{1}{\sqrt{2}} \begin{pmatrix} 1 & -1 \\ -1 & -1 \end{pmatrix},$$

$$\hat{U}_{13} = \frac{1}{\sqrt{2}} \begin{pmatrix} 1 & -i \\ i & -1 \end{pmatrix}, \quad \hat{U}_{24} = \frac{1}{\sqrt{2}} \begin{pmatrix} 1 & i \\ -i & -1 \end{pmatrix},$$

$$\hat{U}_{23} = \frac{1}{2} \begin{pmatrix} \sqrt{3} & e^{-i\pi/6} \\ e^{i\pi/6} & -\sqrt{3} \end{pmatrix}, \quad U_{14} = \frac{1}{2} \begin{pmatrix} 1 & \sqrt{3}e^{-i\pi/3} \\ \sqrt{3}e^{i\pi/3} & -1 \end{pmatrix} \quad (7)$$

These 2×2 unitaries are obtained from Eq. 4 by appropriate settings for δ and α . The most general 4×4 unitary is formed of a concatenation of unitaries in the form of \hat{U}_B and \hat{U}_C [25]. We depict in Fig. 1(f,g) the chip layouts for realizing \hat{U}_B and \hat{U}_C , where we identify the modal pathways with different colors.

IV. RECONSTRUCTING THE COHERENCE MATRIX

A. Modal Stokes parameters for a two-mode field

To elucidate our approach to the reconstruction of a 4×4 coherence matrix representing a four-mode partially coherent field, we first establish the reconstruction of its 2×2 counterpart. A 2×2 Hermitian coherence matrix for modes $|1\rangle$ and $|2\rangle$ is expanded in terms of Pauli matrices, $\mathbf{G} = \frac{1}{2} \sum_{j=0}^3 s_j \hat{\sigma}_j$, where $\hat{\sigma}_0 = \hat{\mathbb{I}}_2$ is the 2×2 identity matrix, and the other Pauli matrices $\{\hat{\sigma}_j\}$ are:

$$\hat{\sigma}_1 = \begin{pmatrix} 1 & 0 \\ 0 & -1 \end{pmatrix}, \quad \hat{\sigma}_2 = \begin{pmatrix} 0 & 1 \\ 1 & 0 \end{pmatrix}, \quad \hat{\sigma}_3 = \begin{pmatrix} 0 & -i \\ i & 0 \end{pmatrix}, \quad (8)$$

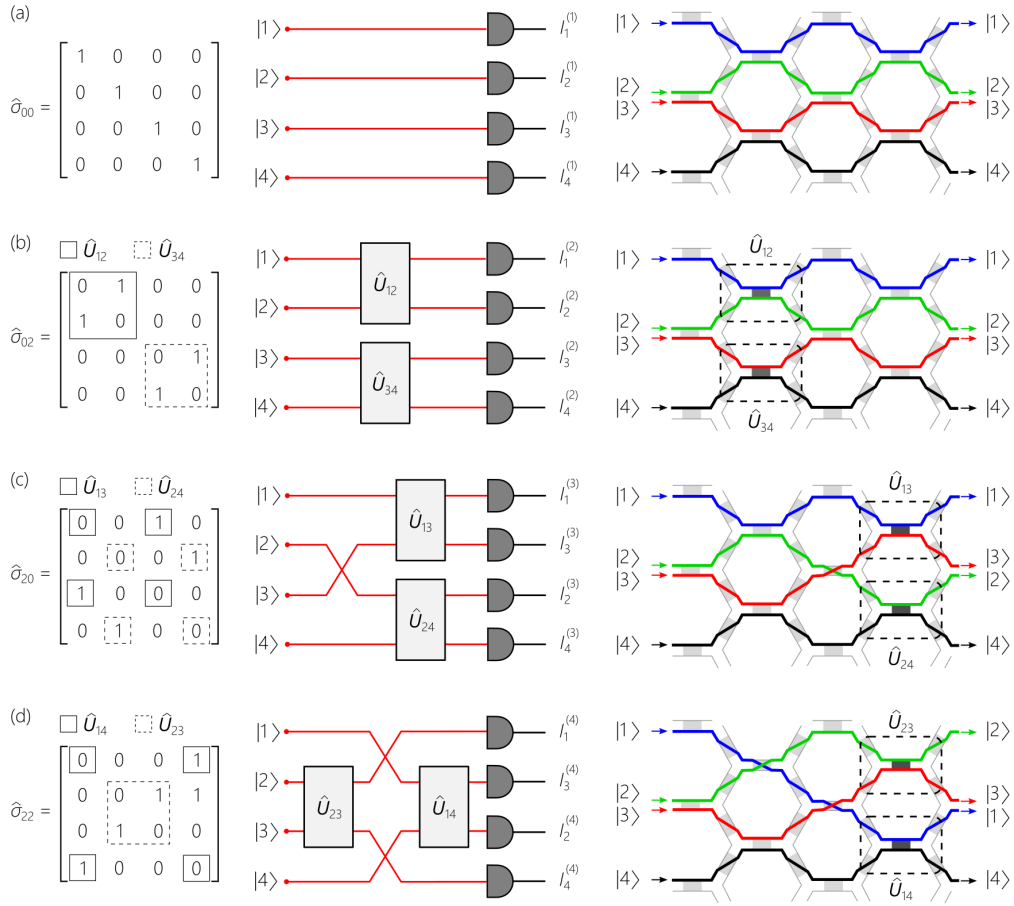


FIG. 2. Reconstructing a 4×4 coherence matrix \mathbf{G} from the modal Stokes parameters. The left column highlights the structure of the relevant 4×4 Kronecker Pauli matrix; the middle shows the conceptual measurement scheme; and the right depicts the corresponding chip layout, with the paths followed by the modes indicated with different colors. (a) Measuring s_{00} , s_{01} , s_{10} , and s_{11} . The Kronecker Pauli matrices $\hat{\sigma}_{00}$, $\hat{\sigma}_{01}$, $\hat{\sigma}_{10}$, and $\hat{\sigma}_{11}$ are diagonal ($\hat{\sigma}_{01} = \hat{\sigma}_0 \otimes \hat{\sigma}_1$ shown). Detectors record the modal weights $I_1^{(1)}$, $I_2^{(1)}$, $I_3^{(1)}$, and $I_4^{(1)}$, and the modal Stokes parameters are obtained using Eq. 12. (b) Measuring s_{02} , s_{03} , s_{12} , and s_{13} . The Kronecker Pauli matrices $\hat{\sigma}_{02}$, $\hat{\sigma}_{03}$, $\hat{\sigma}_{12}$, and $\hat{\sigma}_{13}$ are block diagonal ($\hat{\sigma}_{02} = \hat{\sigma}_0 \otimes \hat{\sigma}_2$ shown). Modal Stokes parameters s_{02} and s_{12} are obtained using Eq. 14 after setting $\hat{U}_{12} = \hat{U}_{34} = \hat{U}_2$, and s_{03} and s_{13} using Eq. 15 after setting $\hat{U}_{12} = \hat{U}_{34} = \hat{U}_3$. (c) Measuring s_{20} , s_{21} , s_{30} , and s_{31} . Modal Stokes parameters s_{20} , s_{21} are obtained using Eq. 17 after setting $\hat{U}_{13} = \hat{U}_{24} = \hat{U}_2$, and s_{30} , s_{31} using Eq. 18 after setting $\hat{U}_{13} = \hat{U}_{24} = \hat{U}_3$. (d) Measuring s_{22} , s_{33} , s_{23} , and s_{32} . Modal Stokes parameters s_{22} and s_{33} are obtained using Eq. 20 after setting $\hat{U}_{23} = \hat{U}_{14} = \hat{U}_2$, and s_{23} and s_{32} using Eq. 21 after setting $\hat{U}_{23} = \hat{U}_{14} = \hat{U}_3$.

so that the real expansion coefficients $s_j = \text{Tr}\{\hat{\sigma}_j \mathbf{G}\}$ are the modal Stokes parameters, which are obtained by measuring the modal weights $I_1 = G_{11}$ and $I_2 = G_{22}$ (the fractions of power associated with the modes $|1\rangle$ and $|2\rangle$) after traversing one of three unitaries: $\hat{U}_1 = \hat{\mathbb{I}}_2$, \hat{U}_2 , and \hat{U}_3 , where:

$$\hat{U}_2 = \frac{1}{\sqrt{2}} \begin{pmatrix} 1 & 1 \\ -1 & 1 \end{pmatrix}, \quad \hat{U}_3 = \frac{1}{\sqrt{2}} \begin{pmatrix} 1 & -i \\ -i & 1 \end{pmatrix}. \quad (9)$$

After $\hat{U}_1 = \hat{\mathbb{I}}_2$, $s_0 = I_1 + I_2$ and $s_1 = I_1 - I_2$; after \hat{U}_2 , $s_2 = I_1 - I_2$, and after \hat{U}_3 , $s_3 = I_1 - I_2$, as demonstrated recently in an on-chip platform [37].

B. Kronecker Pauli matrices and modal Stokes parameters for a four-mode field

We expand the 4×4 coherence matrix \mathbf{G} for 4-mode partially coherent light in terms of 4×4 ‘Kronecker Pauli matrices’ [38]:

$$\mathbf{G} = \frac{1}{4} \sum_{j,k=0}^3 s_{jk} \hat{\sigma}_{jk}, \quad (10)$$

where the 16 Kronecker Pauli matrices are outer products of Pauli matrices (Eq. 8): $\hat{\sigma}_{jk} = \hat{\sigma}_j \otimes \hat{\sigma}_k$ (given explicitly in the Appendix). The modal Stokes parameters s_{jk} are the real expansion coefficients of \mathbf{G} in terms of $\{\hat{\sigma}_{jk}\}$, where $s_{jk} = \text{Tr}\{\hat{\sigma}_{jk} \mathbf{G}\}$. This expansion has been applied to partially coherent optical fields comprising a

pair of binary degrees of freedom (polarization and a pair of spatial modes) [19, 28, 31, 39, 40] (and previously to entangled photon pairs [41, 42], and is applied here to four-mode partially coherent light for the first time to the best of our knowledge.

The 16 Kronecker Pauli matrices can be organized into four sets. The first set comprises diagonal ($\hat{\sigma}_{00}$, $\hat{\sigma}_{01}$, $\hat{\sigma}_{10}$, and $\hat{\sigma}_{11}$), which do not require unitaries for their realization. All that is needed is to directly detect the modal weights: $I_1 = G_{11}$, $I_2 = G_{22}$, $I_3 = G_{33}$, and $I_4 = G_{44}$, and then form the associated Stokes parameters (s_{00} , s_{01} , s_{10} , and s_{11}) from these measurements using Eq. 12 in the Appendix [Fig. 2(a)]. The second set of Kronecker Pauli matrices ($\hat{\sigma}_{02}$, $\hat{\sigma}_{03}$, $\hat{\sigma}_{12}$, and $\hat{\sigma}_{13}$) are block diagonal $\begin{pmatrix} \hat{A} & \hat{0}_2 \\ \hat{0}_2 & \hat{B} \end{pmatrix}$, with \hat{A} and \hat{B} corresponding to $\pm\hat{\sigma}_2$ and $\pm\hat{\sigma}_3$, and $\hat{0}_2$ is a 2×2 matrix with all its elements zero. We implement unitaries \hat{U}_{12} and \hat{U}_{34} on the pairs of modes $\{|1\rangle, |2\rangle\}$ and $\{|3\rangle, |4\rangle\}$, respectively. The modal Stokes parameters associated with $\hat{\sigma}_{02}$ and $\hat{\sigma}_{12}$ (s_{02} and s_{12}) are evaluated by implementing $\hat{U}_{12} = \hat{U}_{34} = \hat{U}_2$, and then using Eq. 14, whereas the modal Stokes parameters associated with $\hat{\sigma}_{03}$ and $\hat{\sigma}_{13}$ (s_{03} and s_{13}) are evaluated by implementing $\hat{U}_{12} = \hat{U}_{34} = \hat{U}_3$, and then using Eq. 15 [Fig. 2(b)].

The remaining 8 Kronecker Pauli matrices have the off-diagonal block-matrix form $\begin{pmatrix} \hat{0}_2 & \hat{A} \\ \hat{B} & \hat{0}_2 \end{pmatrix}$. One group of these ($\hat{\sigma}_{20}$, $\hat{\sigma}_{30}$, $\hat{\sigma}_{21}$, and $\hat{\sigma}_{31}$) requires implementing unitaries \hat{U}_{13} and \hat{U}_{24} on the pairs of modes $\{|1\rangle, |3\rangle\}$ and $\{|2\rangle, |4\rangle\}$, respectively. The modal Stokes parameters associated with Kronecker Pauli matrices $\hat{\sigma}_{20}$ and $\hat{\sigma}_{21}$ (s_{20} and s_{21}) require setting $\hat{U}_{13} = \hat{U}_{24} = \hat{U}_2$ and substituting the modal weights in Eq. 17, and those associated with $\hat{\sigma}_{30}$ and $\hat{\sigma}_{31}$ (s_{30} and s_{31}) require setting $\hat{U}_{13} = \hat{U}_{24} = \hat{U}_3$ and then substituting the modal weights in Eq. 18 [Fig. 2(c)]. Finally, for $\hat{\sigma}_{22}$, $\hat{\sigma}_{23}$, $\hat{\sigma}_{32}$, and $\hat{\sigma}_{33}$ we implement unitaries \hat{U}_{14} and \hat{U}_{23} on the pairs of modes $\{|1\rangle, |4\rangle\}$ and $\{|2\rangle, |3\rangle\}$, respectively. The modal Stokes parameters associated with Kronecker Pauli matrices $\hat{\sigma}_{22}$ and $\hat{\sigma}_{33}$ (s_{22} and s_{33}) require setting $\hat{U}_{14} = \hat{U}_{23} = \hat{U}_2$ and substituting the modal weights in Eq. 20, and those associated with $\hat{\sigma}_{23}$ and $\hat{\sigma}_{32}$ (s_{23} and s_{32}) require setting $\hat{U}_{14} = \hat{U}_{23} = \hat{U}_3$ and substituting the modal weights in Eq. 21 [Fig. 2(d)].

V. MEASUREMENTS

A. Incoherent source of four-mode light

Our source of four-mode incoherent light described by the 4×4 coherence matrix $\mathbf{G} = \frac{1}{4}\hat{\mathbb{I}}_4$ (maximally incoherent light) is depicted in Fig. 3(a). A laser diode at a wavelength $\approx 1.55 \mu\text{m}$ coupled to a single-mode fiber (SMF) is split via a 3-dB fiber coupler into paths a and b . We

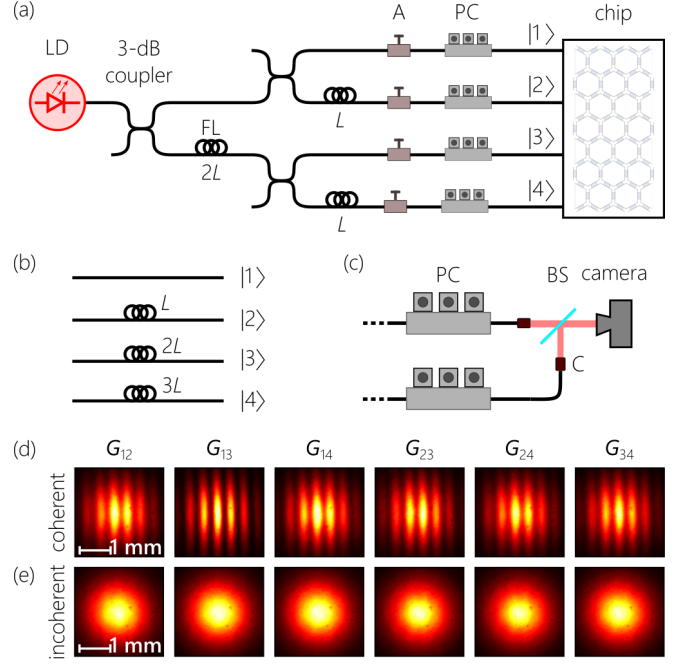


FIG. 3. (a) Source of four-mode incoherent light. LD: Laser diode; FL: fiber loop; A: variable attenuator; PC: polarization controller. (b) The four modes $|1\rangle$, $|2\rangle$, $|3\rangle$, and $|4\rangle$ traverse relative fiber lengths of 0, L , $2L$, and $3L$, respectively, to reach the chip. (c) Setup for interfering a pair of modes. BS: Balanced beam splitter; C: fiber collimator. (d) Measured intensity profiles after superposing pairs of modes in absence of the fiber loops, whereupon the fields are mutually coherent and interference fringes are observed; and (e) in presence of the fiber loops, whereby the fields are mutually incoherent and the interference fringes are eliminated.

place a fiber loop of length $2L$ in path b (with $L \approx 500 \text{ m}$, which far exceeds the laser-diode coherent length). The length L exceeds the fiber coherence length, so the fields in the SMFs no longer interfere at zero relative delay. We next place a 3-dB coupler in a to split it into paths $|1\rangle$ and $|2\rangle$, and a 3-dB coupler in b to split it into paths $|3\rangle$ and $|4\rangle$. We place fiber loops of length L in paths $|2\rangle$ and $|4\rangle$. The lengths of fiber in paths $|1\rangle$, $|2\rangle$, $|3\rangle$, and $|4\rangle$ are 0, L , $2L$, and $3L$, respectively [Fig. 3(b)]. Attenuators placed in each path adjust the power to achieve equal values, and polarization controllers match the polarization to the on-chip waveguides [Fig. 3(a)].

We thus produce four-mode incoherent light confined to four SMFs, which enables efficient coupling to on-chip single-mode waveguides. Any pair of modes are separated by at least a length L [Fig. 3(b)], so that no interference is observed when superposing the two fields. To confirm that such pairs do not exhibit mutual interference, we out-couple the fields from the SMFs through fiber collimators (F220APC-1550, Thorlabs), we overlap the fields corresponding to all six possible pairs of modes at a balanced beam splitter (BS015, Thorlabs), and record the resulting intensity distribution using a camera (Bobcat-320-GigE-13907, Xenics) placed $\approx 30 \text{ cm}$ away

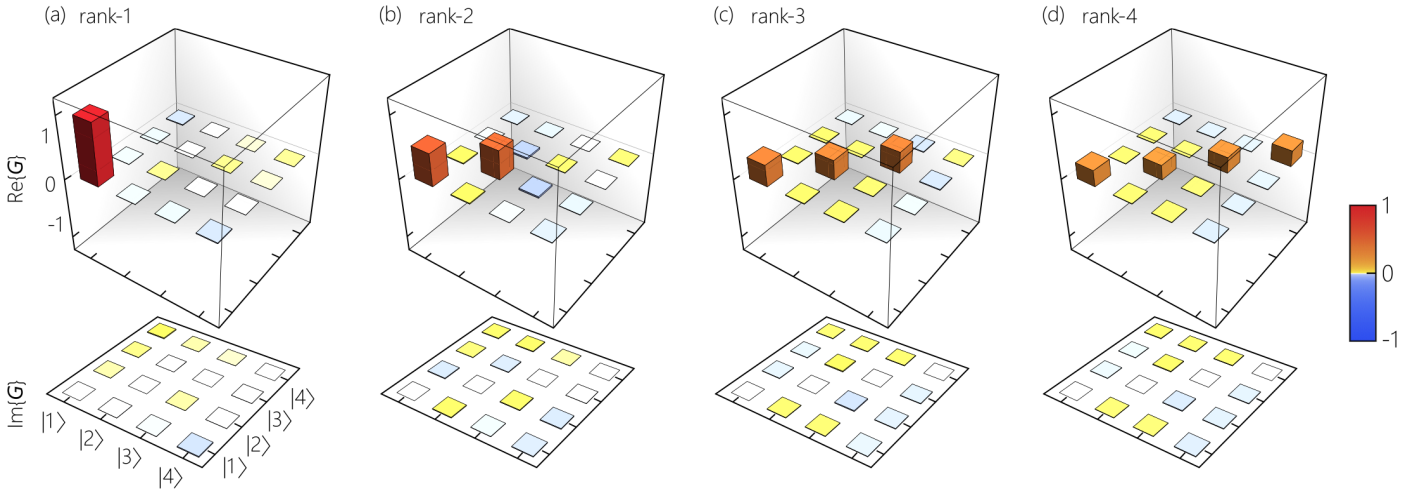


FIG. 4. Measured coherence matrices for maximum-entropy fields of different rank. (a) Rank-1 with $\mathbf{G}_1 = \text{diag}\{1, 0, 0, 0\}$; (b) rank-2 with $\mathbf{G}_2 = \text{diag}\{\frac{1}{2}, \frac{1}{2}, 0, 0\}$; (c) rank-3 with $\mathbf{G}_3 = \text{diag}\{\frac{1}{3}, \frac{1}{3}, \frac{1}{3}, 0\}$; and (d) rank-4 with $\mathbf{G}_4 = \text{diag}\{\frac{1}{4}, \frac{1}{4}, \frac{1}{4}, \frac{1}{4}\}$. We plot separately the real and imaginary parts of the coherence matrices, $\text{Re}\{\mathbf{G}\}$ and $\text{Im}\{\mathbf{G}\}$, respectively.

from the collimators. We plot in Fig. 3(d) the measurements after removing the fiber loops, where we observe high-visibility fringes as expected for the overlap of fields derived from the same source. In contrast, the interference fringes are eliminated in presence of the fiber loops, indicating their mutual incoherence. The visibility V_{jk} for any pair of modes $|j\rangle$ and $|k\rangle$ is related to the corresponding off-diagonal element of \mathbf{G} , $V_{jk} = \frac{2|G_{jk}|}{G_{jj} + G_{kk}}$ when $\text{Tr}\{\mathbf{G}\} = 1$. The absence of interference for all six pairs of modes confirms that the off-diagonal elements of \mathbf{G} are all zero, thus confirming that an incoherent field with $\mathbf{G} = \frac{1}{4}\hat{\mathbb{I}}_4$ is delivered to the chip.

B. Controlling the coherence rank

The first task is on-chip control of the coherence rank. Starting with the rank-4 field $\mathbf{G}_4 = \text{diag}\{\frac{1}{4}, \frac{1}{4}, \frac{1}{4}, \frac{1}{4}\}$ prepared off-chip, changing the rank requires changing the amplitudes of the diagonal elements of \mathbf{G} , which is a non-unitary operation realized via an MZI in the path of each mode. For example, directing mode $|4\rangle$ to one input port of an MZI [Fig. 1(b), Eq. 4] and providing no input to the other input port reduces the modal weight for $|4\rangle$ by $\sin^2(\frac{\delta}{2})$ (discarding the other output). Setting $\delta = 0$, we eliminate the mode $|4\rangle$ altogether ($\lambda_4 = 0$), thereby yielding a rank-3 field with $\mathbf{G}_3 = \text{diag}\{\frac{1}{3}, \frac{1}{3}, \frac{1}{3}, 0\}$. When the modal weights for both modes $|3\rangle$ and $|4\rangle$ are eliminated ($\lambda_3 = \lambda_4 = 0$), we obtain a rank-2 field with $\mathbf{G}_2 = \text{diag}\{\frac{1}{2}, \frac{1}{2}, 0, 0\}$. Carrying out this procedure for modes $|2\rangle$, $|3\rangle$, and $|4\rangle$ ($\lambda_2 = \lambda_3 = \lambda_4 = 0$) yields a coherent rank-1 field with $\mathbf{G}_1 = \text{diag}\{1, 0, 0, 0\}$.

To reconstruct the coherence matrix \mathbf{G} , we program the chip to sequentially implement the four layouts depicted in Fig. 2 (right column). In each configuration the modal weights are recorded with on-chip de-

tectors, and four modal Stokes parameters are obtained (Appendix). The 16 modal Stokes parameters s_{jk} are substituted into Eq. 10 to reconstruct \mathbf{G} . We quantify the quality of the measured coherence matrix \mathbf{G}_{meas} with respect to the theoretically expected coherence matrix $\mathbf{G}_{\text{theory}}$ coherence matrices using the fidelity $F = (\text{Tr}\{\sqrt{\mathbf{G}_{\text{meas}}}\mathbf{G}_{\text{theory}}\sqrt{\mathbf{G}_{\text{meas}}}\})^2$ [43]. The measurement results for on-chip control of the coherence rank are given in Fig. 4. We plot the reconstructed coherence matrices of ranks 1, 2, 3, and 4 separating the real and imaginary parts, $\text{Re}\{\mathbf{G}\}$ and $\text{Im}\{\mathbf{G}\}$, respectively. In all 4 cases we find negligible imaginary components, and predominantly diagonal contributions to the real part of \mathbf{G} . The average fidelity is $F \approx 0.95$ for the reconstructed coherence matrices of rank-1, rank-2, and rank-3, and $F \approx 0.99$ for rank-4. We attribute the lower fidelity to leakage of the modal amplitude from the MZIs that are utilized to extinguish the corresponding modal amplitudes, whereas the rank-4 field does not require that feature (all the modal amplitudes coupled to the chip enter the coherence-matrix reconstruction stage).

C. Tuning the entropy of the coherence matrix

On-chip tuning of the entropy $S(\mathbf{G})$ for a coherence matrix \mathbf{G} of given rank requires controllably modifying the relative weights of the eigenvalues (Eq. 3). We can perform this task using the same MZIs that we relied on to tune the coherence rank. However, rather than eliminating the eigenvalue altogether (when the coherence matrix is in diagonal form), we set the value of the parameter δ in Eq. 4 to adjust each eigenvalue by a factor $\sin^2(\frac{\delta_j}{2})$, where δ_j is the MZI parameter for the mode $|j\rangle$, $j = 1, 2, 3, 4$.

Rank-1 fields have $S = 0$, which cannot be tuned once

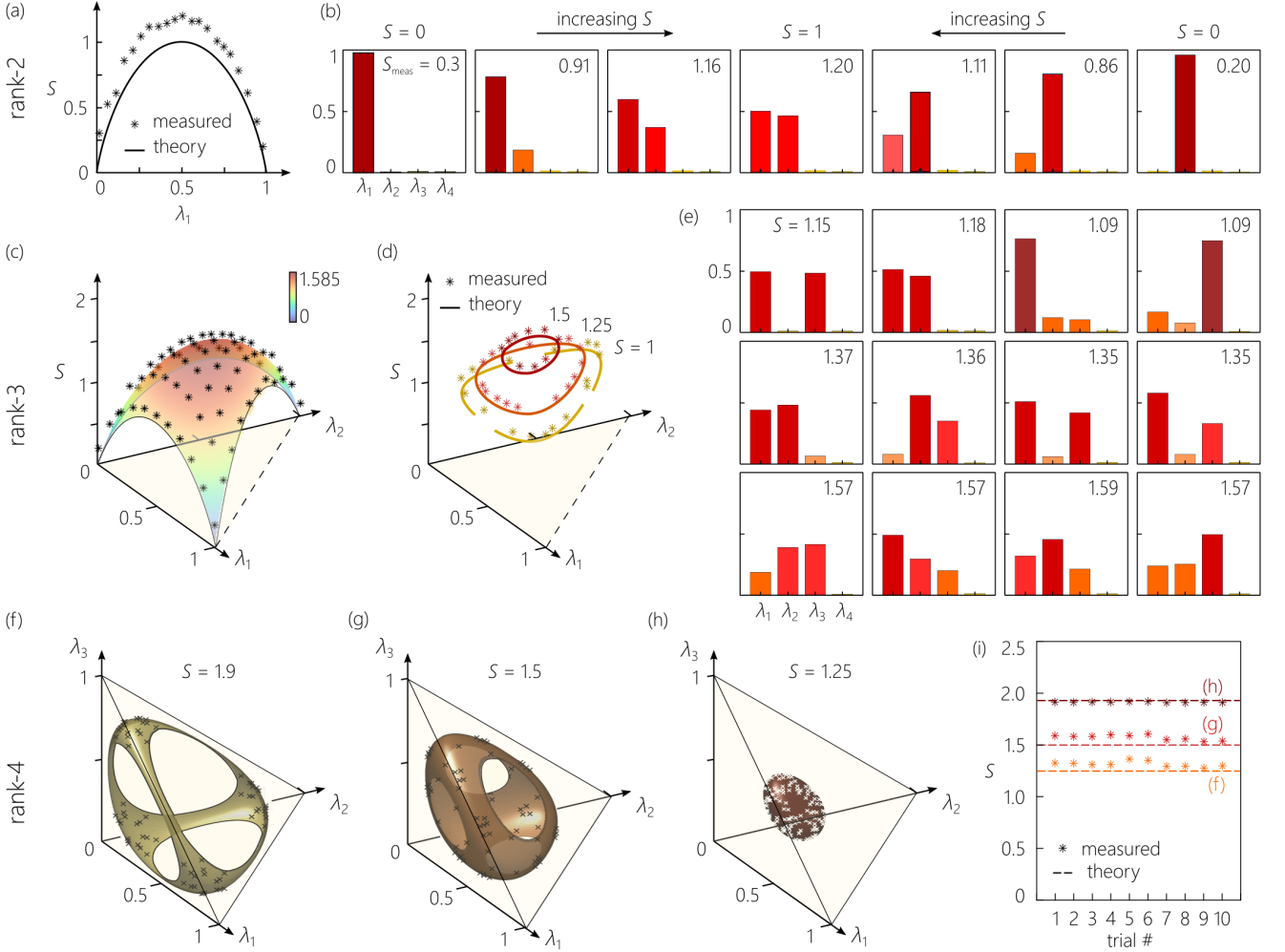


FIG. 5. On-chip tuning of the entropy of a four-mode partially coherent field. (a) Measured entropy $S(\lambda_1)$ for rank-2 fields as we vary the eigenvalue λ_1 from 0 to 1 ($\lambda_2 = 1 - \lambda_1$, $\lambda_3 = \lambda_4 = 0$). The curve is the theoretical expectation, the points are measurements. (b) Samples of the eigenvalues of the reconstructed coherence matrices as we vary λ_1 . (c) The measured entropy $S(\lambda_1, \lambda_2)$ for rank-3 fields as points overlaid on the theoretical surface. We vary λ_1 and λ_2 from 0 to 1, $\lambda_3 = 1 - \lambda_1 - \lambda_2$ and $\lambda_4 = 0$. (d) Measured entropy for iso-entropy rank-3 fields plotted along with the theoretical curves for $S = 1, 1.25$, and 1.5 bits. (e) Samples of the extracted eigenvalues from reconstructed iso-entropy coherence matrices corresponding to (d). (f) The measured entropy for iso-entropy rank-4 fields with $S = 1.9$ bits (plotted as black points) overlaid on the theoretically expected iso-entropy surface. (g) Same as (f) for $S = 1.5$ bits, and (h) for $S = 1.25$ bits. In the latter, the measurements points are white for clarity. (i) The measured entropy for 10 reconstructed coherence matrices selected from (f-h) compared to the target entropy values.

we set $\lambda_2 = \lambda_3 = \lambda_4 = 0$; changing the amplitude of the remaining modal amplitude associated with $|1\rangle$ does not change S . Rank-2 fields with $\mathbf{G} = \text{diag}\{\lambda_1, \lambda_2, 0, 0\}$ have entropy $0 < S \leq 1$. We carry out measurements by eliminating λ_3 and λ_4 and then tuning the values of λ_1 and λ_2 from 0 to 1, with $\lambda_1 + \lambda_2 = 1$. We plot the measured entropy for the reconstructed coherence matrices as points in Fig. 5(a), along with the theoretical curve $S = -\lambda_1 \log_2 \lambda_1 - \lambda_2 \log_2 \lambda_2$. In addition, we plot in Fig. 5(b) eigenvalues $\{\lambda_1, \lambda_2, \lambda_3, \lambda_4\}$ extracted from a selection of reconstructed coherence matrices. We note that the measured entropy is consistently higher than the theoretical expectation. Note that the recon-

structed eigenvalues deviate only a few percent from theory; for example, in the first coherence matrix in Fig. 5(b) we have $\lambda_1 \approx 0.98$ (rather than $\lambda_1 = 1$) and $\lambda_2 + \lambda_3 + \lambda_4 \approx 0.02$ (rather than 0). This small deviation leads to a large shift in entropy (from 0 to ≈ 0.2 bit) because of the sensitivity of the logarithm function. The deviation is due to amplitude leakage from the MZI's used to control the relative modal weights (the amplitude is not completely extinguished as required), which requires furthermore improvements.

Crucially, the entropy S for a rank-2 field uniquely identifies the two eigenvalues [44]. Any pair of rank-2 coherence matrices having equal entropy can be inter-

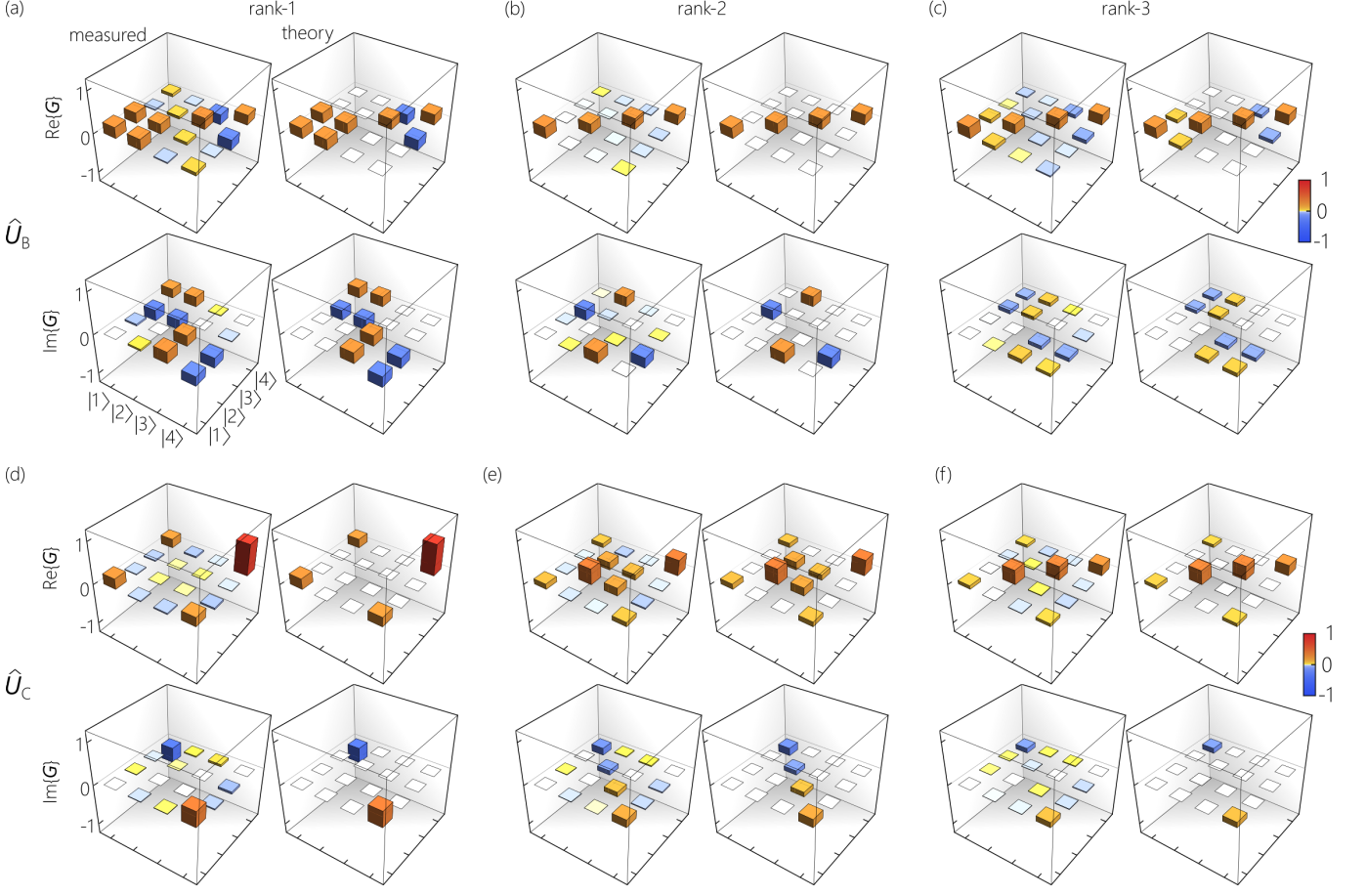


FIG. 6. Measured \mathbf{G} for rank-1, rank-2, and rank-3 fields from Fig. 4 after traversing the unitaries \hat{U}_B and \hat{U}_C . (a) The real and imaginary parts of the rank-1 coherence matrix $\mathbf{G} = \text{diag}\{1, 0, 0, 0\}$ after traversing \hat{U}_B . The left column in the panel is the measured coherence matrix, and the right column is the theoretically expected counterpart. (b) Same as (a) for the rank-2 coherence matrix $\mathbf{G} = \text{diag}\{\frac{1}{2}, \frac{1}{2}, 0, 0\}$ after traversing \hat{U}_B . (c) Same as (a) for the rank-3 coherence matrix $\mathbf{G} = \text{diag}\{\frac{1}{3}, \frac{1}{3}, \frac{1}{3}, 0\}$ after traversing \hat{U}_B . (d-f) Same as (a-c) for the three fields of ranks 1, 2, and 3 after traversing \hat{U}_C .

converted unitarily. Conversely, any two coherence matrices that can be inter-converted unitarily have the same entropy [44]. This property does *not* extend to rank-3 fields: entropy no longer identifies a coherence matrix to within a unitary [28]. Indeed, any rank-3 coherence matrices \mathbf{G}_3 and \mathbf{G}'_3 that can be inter-converted unitarily $\mathbf{G}'_3 = \hat{U}\mathbf{G}_3\hat{U}^\dagger$ have the same entropy, $S(\mathbf{G}_3) = S(\mathbf{G}'_3)$. However, the opposite is *not* guaranteed: two rank-3 coherence matrices \mathbf{G}_3 and \mathbf{G}'_3 having equal entropy $S(\mathbf{G}_3) = S(\mathbf{G}'_3)$ are not guaranteed to be inter-converted into each other unitarily. In such a case where the two iso-entropy rank-3 fields cannot be inter-converted unitarily, non-unitary transformations are required, typically involving modal filtering and decohering [28].

We tuned the entropy of rank-3 fields ($\lambda_4 = 0$) by sweeping the values of λ_1 , λ_2 , and λ_3 : λ_1 is swept over the range from 0 to 1, λ_2 is swept from 0 to $1 - \lambda_1$, and $\lambda_3 = 1 - \lambda_1 - \lambda_2$. This is accomplished using MZIs associated with the modal weights of $|1\rangle$, $|2\rangle$, and $|3\rangle$. The measured entropy obtained from the reconstructed rank-

3 coherence matrices are plotted as points in Fig. 5(c) along with the theoretical surface $S = -\sum_{j=1}^3 \lambda_j \log_2 \lambda_j$. We plot the measurements and the theoretical surface in Fig. 5(c) over a right-angled triangular domain in the (λ_1, λ_2) -plane delimited by the line $\lambda_1 + \lambda_2 = 1$ (representing the rank-2 limit of rank-3 fields, $\lambda_3 \rightarrow 2$). The entropy surface reaches $S = 0$ at the vertices of the triangle ($\lambda_2 = 0, \lambda_3 = 0$, or $\lambda_1 = \lambda_2 = 0$), and reaches a peak of $S = \log_2 3 \approx 1.585$ at $\lambda_1 = \lambda_2 = \frac{1}{3}$. Any point on this surface represents all the coherence matrices that can be inter-converted into each other unitarily. All the measured values of S across the entire domain are in close proximity to the theoretical surface.

To confirm the versatility of on-chip entropy tuning, we vary the modal weights of $|1\rangle$, $|2\rangle$, and $|3\rangle$ to produce iso-entropy fields that cannot be inter-converted unitarily. Such fields are represented in the space depicted in Fig. 5(c) by the points on a curve at the intersection of the surface for S with a horizontal plane corresponding to fixed entropy. The curve becomes a point when

$S \rightarrow \log_2 3$, and its area grows with decreasing S to reach a maximum when $S = 1$, whereupon it is tangential to the three sides of the base triangle. When $S < 1$, the curve breaks up into disjoint segments in the vicinity of the vertices of the base triangle. We select $S = 1, 1.25$, and 1.5 bits, and produce iso-entropy coherence matrices at these three values. The entropy obtained from the reconstructed coherence matrices are plotted as points along with the iso-entropy curves in Fig. 5(d). Examples of the eigenvalues extracted from the reconstructed coherence matrices associated with these fixed entropy values are given in Fig. 5(e). For each value of S , the iso-entropy coherence matrices have different eigenvalues and thus cannot be inter-converted unitarily.

To tune the entropy of rank-4 fields, we engage all 4 MZIs associated with the modes to control their corresponding eigenvalues. Diagonal rank-4 fields have three independent parameters after enforcing the constraints $\sum_{j=1}^4 \lambda_j = 1$ and $0 \leq \lambda_j \leq 1$ on the eigenvalues. A plot of the entropy for general rank-4 coherence matrices therefore cannot be readily visualized. We thus pursue instead iso-entropy rank-4 fields. The fixed entropy yields an additional constraint that restricts the family of rank-4 fields to a surface in $(\lambda_1, \lambda_2, \lambda_3)$ -space [Fig. 5(f-h)]. Any rank-4 coherence matrix can be represented by a point in $(\lambda_1, \lambda_2, \lambda_3)$ -space within the triangular pyramid shown in Fig. 5(f-h). Points on the facets correspond to rank-3 fields, points along the edges correspond to rank-2 fields, and the vertices are rank-1 fields. In Fig. 5(f) we plot the theoretical iso-entropy surface corresponding to $S = 1.9$ bits. Because $S = 1.9 > \log_2 3$, only rank-4 fields can attain this value, and the surface lies within the volume of the triangular pyramid (no rank-2 or rank-3 fields can attain this value of entropy). The points are correspond to reconstructed coherence matrices at this entropy value, which all lie within the vicinity of the theoretical surface. Measurement results for iso-entropy rank-4 fields with $S = 1.5$ bits are plotted in Fig. 5(g) along with the theoretical iso-entropy surface, which now intersects with the facets of the volume (rank-3 fields can attain $S = 1.5$ bits, but not rank-2). The corresponding measurements for $S = 1.25$ bits are plotted in Fig. 5(h). Finally, the measured entropy for all the reconstructed coherence matrices in Fig. 5(f-h) are collected in Fig. 5(i) to facilitate comparison with the theoretical targets. In general, the data for rank-4 fields is is stronger agreement with theoretical expectations than rank-2 and rank-3 fields that require complete extinguishing of on-chip modal amplitudes.

D. Unitary transformations

After on-chip tuning of the rank and entropy of the four-mode coherence matrix via non-unitary transformations, we proceed to modify the structure of the coherence matrix via unitary transformations. We implement the 4×4 unitaries \hat{U}_B and \hat{U}_C (Eq. 6), whose layouts are

depicted in Fig. 1(f,g). We direct to these two unitaries the fields corresponding to diagonal coherence matrices, \mathbf{G}_1 through \mathbf{G}_4 , corresponding to ranks 1 through 4. We plot the reconstructed coherence matrix and the theoretical expectation (separating their real and imaginary parts) after \mathbf{G}_1 traverses \hat{U}_B in Fig. 6(a), after \mathbf{G}_2 traverses \hat{U}_B in Fig. 6(b), and \mathbf{G}_3 traverses \hat{U}_B in Fig. 6(c). The corresponding results after \mathbf{G}_1 , \mathbf{G}_2 , and \mathbf{G}_3 traverse \hat{U}_C in Fig. 6(d-f). The unitaries were selected to mold the structure of the on-chip prepared diagonal coherence matrices and prepare new coherence matrices (having the same rank and entropy) but whose off-diagonal elements are appreciable, indicating that correlations have been introduced between the modes, so that they can now exhibit interference when superposed – in contrast to the correlation-free state introduced into the chip as evinced in Fig. 3(e). Moreover, the unitaries transform the coherence matrices to have significant imaginary off-diagonal values, indicating tunability of the phase of the correlation between the modes. The average fidelity of the reconstructed coherence matrices is $F \approx 0.95$. For the rank-4 field $\mathbf{G}_4 = \frac{1}{4}\hat{\mathbb{I}}_4$, the unitaries \hat{U}_B and \hat{U}_C leave the coherence matrix invariant as expected, $\hat{U}\mathbf{G}_4\hat{U}^\dagger = \mathbf{G}_4$. In all cases, the fidelity F exceeds ≈ 0.95 . These results confirm the feasibility of modifying the structure of 4×4 coherence matrices via unitaries in an integrated photonics platform.

VI. DISCUSSION AND CONCLUSION

Our results here provide the first experimental confirmation for the scalability of on-chip manipulation of multimode partially coherent light using basic building blocks that transform pairs of modes at a time. This conclusion with regards to scalability extends to all the facets necessary for full control over partially coherent light in an integrated-photonics platform with intended utility in optical information processing. First, our approach for the efficient coupling of partially coherent light to single-mode on-chip waveguides can be readily expanded to $N \geq 4$ modes by using a larger number of fiber couplers and delays, with the potential addition of fiber amplifiers if needed. Second, on-chip control of the coherence rank requires only a single element (an MZI or a switch) per mode to selectively eliminate the corresponding modal weight. Third, the field entropy can be tuned on chip using a single MZI per mode to precisely modify the corresponding modal weight. Both of these tasks, controlling the coherence rank and tuning the field entropy, are linear non-unitary operations that can be readily extended to $N \geq 4$ modes. Fourth, the structure of the $N \times N$ coherence matrix can be molded on chip through concatenation of 2×2 unitary building blocks [25, 45, 46] – as long as a sufficient number of on-chip building blocks are available – utilizing the approach that has been well-established in mathematics, quantum optics, and programmable photonics [22].

Fifth, tomographic reconstruction of the $N \times N$ Hermitian coherence matrix can be extended to $N \geq 4$ utilizing Kronecker Pauli matrices of corresponding dimension, which in turn determine the requisite measurements for the modal Stokes parameters.

Several open questions need to be addressed to further the utility of programmable photonics for manipulating partially coherent light. First, optimizing the leakage from MZIs is necessary for precise tuning of the field entropy (which is not a problem for coherent light). Second, whereas the reconstruction of $N \times N$ coherence matrices is straightforward for N even, odd-dimensional modal basis requires adopting a different matrix decomposition of the coherence matrix, likely by utilizing Gell-Mann matrices, which generate the elements of the unitary matrix group $SU(3)$ [47], as the Pauli matrices generate the elements of $SU(2)$. Third, as the dimension N increases, the speed of coherence-matrix reconstruction will become a bottleneck. This requires a careful comparison of the modal-Stokes-parameters reconstruction strategy presented here (see also [35, 39, 40], which requires a fixed number of N^2 measurements carried out on any $N \times N$ coherence matrix, and the variational strategy outlined theoretically in Ref. [48], possibly augmented with machine-learning algorithms for speed-up.

Our findings pave the way to the preparation of multimode structured coherence to be launched from integrated-photonics platforms into free space or multimode fibers and exploit the coherence advantage in optical [17, 19] or millimeter wave [49] communications. The results reported here validate the utility of programmable photonics in manipulating partially coherent light for fundamental studies of entropy concentration and swapping [28, 30, 31, 50], and in high-speed applications in secure optical communications [51, 52], sensing [16, 53], cryptography [54, 55], computation [18], and spectroscopy [20].

APPENDIX: MEASURING THE MODAL STOKES PARAMETERS OG FOUR-MODE PARTIALLY COHERENT LIGHT

The Kronecker Pauli matrices $\{\hat{\sigma}_{jk}\}$ are direct products of Pauli matrices. The Kronecker Pauli matrices $\hat{\sigma}_{00}$, $\hat{\sigma}_{01}$, $\hat{\sigma}_{10}$, and $\hat{\sigma}_{11}$ are:

$$\begin{aligned}\hat{\sigma}_{00} &= \begin{pmatrix} 1 & 0 & 0 & 0 \\ 0 & 1 & 0 & 0 \\ 0 & 0 & 1 & 0 \\ 0 & 0 & 0 & 1 \end{pmatrix}, \hat{\sigma}_{01} = \begin{pmatrix} 1 & 0 & 0 & 0 \\ 0 & -1 & 0 & 0 \\ 0 & 0 & 1 & 0 \\ 0 & 0 & 0 & -1 \end{pmatrix}, \\ \hat{\sigma}_{10} &= \begin{pmatrix} 1 & 0 & 0 & 0 \\ 0 & 1 & 0 & 0 \\ 0 & 0 & -1 & 0 \\ 0 & 0 & 0 & -1 \end{pmatrix}, \hat{\sigma}_{11} = \begin{pmatrix} 1 & 0 & 0 & 0 \\ 0 & -1 & 0 & 0 \\ 0 & 0 & -1 & 0 \\ 0 & 0 & 0 & 1 \end{pmatrix}\end{aligned}\quad (11)$$

which are diagonal, so that they correspond to direct measurements of the modal weights $I_j^{(1)}$ [Fig. 2(a)], from

which the associated modal Stokes parameters s_{00} , s_{01} , s_{10} , and s_{11} can be evaluated as follows:

$$\begin{aligned}s_{00} &= I_1^{(1)} + I_2^{(1)} + I_3^{(1)} + I_4^{(1)}, \\ s_{01} &= I_1^{(1)} - I_2^{(1)} + I_3^{(1)} - I_4^{(1)}, \\ s_{10} &= I_1^{(1)} + I_2^{(1)} - I_3^{(1)} - I_4^{(1)}, \\ s_{11} &= I_1^{(1)} - I_2^{(1)} - I_3^{(1)} + I_4^{(1)}.\end{aligned}\quad (12)$$

The Kronecker Pauli matrices $\hat{\sigma}_{02}$, $\hat{\sigma}_{03}$, $\hat{\sigma}_{12}$, and $\hat{\sigma}_{13}$ are:

$$\begin{aligned}\hat{\sigma}_{02} &= \begin{pmatrix} 0 & 1 & 0 & 0 \\ 1 & 0 & 0 & 0 \\ 0 & 0 & 0 & 1 \\ 0 & 0 & 1 & 0 \end{pmatrix}, \hat{\sigma}_{03} = \begin{pmatrix} 0 & -i & 0 & 0 \\ i & 0 & 0 & 0 \\ 0 & 0 & 0 & -i \\ 0 & 0 & i & 0 \end{pmatrix}, \\ \hat{\sigma}_{12} &= \begin{pmatrix} 0 & 1 & 0 & 0 \\ 1 & 0 & 0 & 0 \\ 0 & 0 & 0 & -1 \\ 0 & 0 & -1 & 0 \end{pmatrix}, \hat{\sigma}_{13} = \begin{pmatrix} 0 & -i & 0 & 0 \\ i & 0 & 0 & 0 \\ 0 & 0 & 0 & i \\ 0 & 0 & -i & 0 \end{pmatrix}\end{aligned}\quad (13)$$

which have the block diagonal form $\begin{pmatrix} \hat{A} & \hat{\mathbf{0}}_2 \\ \hat{\mathbf{0}}_2 & \hat{B} \end{pmatrix}$, with \hat{A} and \hat{B} corresponding to $\pm\hat{\sigma}_2$ and $\pm\hat{\sigma}_3$. The associated modal Stokes parameters s_{02} , s_{03} , s_{12} , and s_{13} are obtained by implementing unitaries \hat{U}_{12} and \hat{U}_{34} and recording the modal weights $I_j^{(2)}$; setting $\hat{U}_{12} = \hat{U}_{34} = \hat{U}_2$ yields:

$$\begin{aligned}s_{02} &= I_1^{(2)} - I_2^{(2)} + I_3^{(2)} - I_4^{(2)}, \\ s_{12} &= I_1^{(2)} - I_2^{(2)} - I_3^{(2)} + I_4^{(2)},\end{aligned}\quad (14)$$

and setting $\hat{U}_{12} = \hat{U}_{34} = \hat{U}_3$ yields:

$$\begin{aligned}s_{03} &= I_1^{(2)} - I_2^{(2)} + I_3^{(2)} - I_4^{(2)}, \\ s_{13} &= I_1^{(2)} - I_2^{(2)} - I_3^{(2)} + I_4^{(2)}.\end{aligned}\quad (15)$$

The Kronecker Pauli matrices $\hat{\sigma}_{20}$, $\hat{\sigma}_{21}$, $\hat{\sigma}_{30}$, and $\hat{\sigma}_{31}$ are:

$$\begin{aligned}\hat{\sigma}_{20} &= \begin{pmatrix} 0 & 0 & 1 & 0 \\ 0 & 0 & 0 & 1 \\ 1 & 0 & 0 & 0 \\ 0 & 1 & 0 & 0 \end{pmatrix}, \hat{\sigma}_{21} = \begin{pmatrix} 0 & 0 & 1 & 0 \\ 0 & 0 & 0 & -1 \\ 1 & 0 & 0 & 0 \\ 0 & -1 & 0 & 0 \end{pmatrix}, \\ \hat{\sigma}_{30} &= \begin{pmatrix} 0 & 0 & -i & 0 \\ 0 & 0 & 0 & -i \\ i & 0 & 0 & 0 \\ 0 & i & 0 & 0 \end{pmatrix}, \hat{\sigma}_{31} = \begin{pmatrix} 0 & 0 & -i & 0 \\ 0 & 0 & 0 & i \\ i & 0 & 0 & 0 \\ 0 & -i & 0 & 0 \end{pmatrix}\end{aligned}\quad (16)$$

which have the off-diagonal block-matrix form $\begin{pmatrix} \hat{\mathbf{0}}_2 & \hat{A} \\ \hat{B} & \hat{\mathbf{0}}_2 \end{pmatrix}$. To measure the associated modal Stokes parameters s_{20} and s_{21} we implement unitaries \hat{U}_{13} and \hat{U}_{24} and record the modal weights $I_j^{(3)}$ [Fig. 2(c)]; setting $\hat{U}_{13} = \hat{U}_{24} = \hat{U}_2$ yields:

$$\begin{aligned}s_{20} &= I_1^{(3)} + I_2^{(3)} - I_3^{(3)} - I_4^{(3)}, \\ s_{21} &= I_1^{(3)} - I_2^{(3)} - I_3^{(3)} + I_4^{(3)};\end{aligned}\quad (17)$$

and setting $\hat{U}_{13} = \hat{U}_{24} = \hat{U}_3$ yields:

$$\begin{aligned} s_{30} &= I_1^{(3)} + I_2^{(3)} - I_3^{(3)} - I_4^{(3)}, \\ s_{31} &= I_1^{(3)} - I_2^{(3)} - I_3^{(3)} + I_4^{(3)}. \end{aligned} \quad (18)$$

Finally, the Kronecker Pauli matrices $\hat{\sigma}_{22}$, $\hat{\sigma}_{23}$, $\hat{\sigma}_{32}$, and $\hat{\sigma}_{33}$ are:

$$\begin{aligned} \hat{\sigma}_{22} &= \begin{pmatrix} 0 & 0 & 0 & 1 \\ 0 & 0 & 1 & 0 \\ 0 & 1 & 0 & 0 \\ 1 & 0 & 0 & 0 \end{pmatrix}, \hat{\sigma}_{23} = \begin{pmatrix} 0 & 0 & 0 & -i \\ 0 & 0 & i & 0 \\ 0 & -i & 0 & 0 \\ i & 0 & 0 & 0 \end{pmatrix}, \\ \hat{\sigma}_{32} &= \begin{pmatrix} 0 & 0 & 0 & -i \\ 0 & 0 & -i & 0 \\ 0 & i & 0 & 0 \\ i & 0 & 0 & 0 \end{pmatrix}, \hat{\sigma}_{33} = \begin{pmatrix} 0 & 0 & 0 & -1 \\ 0 & 0 & 1 & 0 \\ 0 & 1 & 0 & 0 \\ -1 & 0 & 0 & 0 \end{pmatrix} \end{aligned} \quad (19)$$

which again have off-diagonal block-matrix form. The associated modal Stokes parameters s_{22} , s_{23} , s_{32} , and s_{33} require implementing unitaries \hat{U}_{14} and \hat{U}_{23} and recording the modal weights $I_j^{(4)}$ [Fig. 2(d)]; setting $\hat{U}_{14} = \hat{U}_{23} = \hat{U}_2$ yields:

$$\begin{aligned} s_{22} &= I_1^{(4)} + I_2^{(4)} - I_3^{(4)} - I_4^{(4)}, \\ s_{33} &= -I_1^{(4)} + I_2^{(4)} - I_3^{(4)} + I_4^{(4)}, \end{aligned} \quad (20)$$

and setting $\hat{U}_{14} = \hat{U}_{23} = \hat{U}_3$ yields:

$$\begin{aligned} s_{23} &= I_1^{(4)} - I_2^{(4)} + I_3^{(4)} - I_4^{(4)}, \\ s_{32} &= I_1^{(4)} + I_2^{(4)} - I_3^{(4)} - I_4^{(4)}. \end{aligned} \quad (21)$$

[1] A. A. Michelson, On the application of interference methods to astronomical measurements, *Phil. Mag.* **30**, 1 (1890).

[2] A. A. Michelson, On the application of interference methods to spectroscopic measurements, *Phil. Mag.* **31**, 338 (1891).

[3] F. Zernicke, The concept of the degree of coherence and its application to optical problems, *Physica* **5**, 785 (1938).

[4] L. Mandel and E. Wolf, Coherence properties of optical fields, *Rev. Mod. Phys.* **37**, 231 (1965).

[5] E. Wolf, Optics in terms of observable quantities, *Nuovo Cimento C* **12**, 884 (1954).

[6] E. Wolf, A macroscopic theory of interference and diffraction of light from finite sources II. Fields with a spectral range of arbitrary width, *Proc. Royal Soc. London* **230**, 246 (1955).

[7] E. Wolf, Coherence properties of partially polarized electromagnetic radiation, *Il Nuovo Cimento* **13**, 1165 (1959).

[8] B. Karczewski, Coherence theory of the electromagnetic field, *Il Nuovo Cimento* **30**, 5464 (1963).

[9] J. Peřina, *Coherence of Light* (Van Nostrand, 1972).

[10] E. Wolf, *Introduction to the Theory of Coherence and Polarization of Light* (Cambridge Univ. Press, Cambridge, 2007).

[11] G. S. Agarwal and A. Classen, Partial coherence in modern optics: Emil Wolf's legacy in the 21st century, *Prog. Opt.* **65**, 13 (2020).

[12] G. Gbur and E. Wolf, Spreading of partially coherent beams in random media, *J. Opt. Soc. Am. A* **19**, 1592 (2002).

[13] S. A. Ponomarenko and E. Wolf, Solution of the inverse scattering problem for stringly fluctuating media, *Opt. Lett.* **27**, 1770 (2002).

[14] A. Dogariu and S. Amarande, Propagation of partially coherent beams: turbulence-induced degradation, *Opt. Lett.* **28**, 10 (2003).

[15] E. Baleine and A. Dogariu, Variable-coherence tomography for inverse scattering problems, *J. Opt. Soc. Am. A* **21**, 1917 (2004).

[16] B. Redding, M. A. Choma, and H. Cao, Speckle-free laser imaging using random laser illumination, *Nat. Photon.* **6**, 355 (2012).

[17] A. Nardi, S. Divitt, M. Rossi, F. Tebbenjohanns, A. Militaru, M. Frimmer, and L. Novotny, Encoding information in the mutual coherence of spatially separated light beams, *Opt. Lett.* **47**, 4588 (2022).

[18] B. Dong, F. Brückerhoff-Plückelmann, L. Meyer, J. Dijkstra, I. Bente, D. Wendland, A. Varri, S. Aggarwal, N. Farmakidis, M. Wang, G. Yang, J. S. Lee, Y. He, E. Gooskens, D.-L. Kwong, P. Bienstman, W. H. P. Pernice, and H. Bhaskaran, Partial coherence enhances parallelized photonic computing, *Nature* **632**, 55 (2024).

[19] M. Harling, C. Stevenson, K. C. Toussaint, and A. F. Abouraddy, Optical communications through highly scattering channels using the coherence-rank, *APL Photonics* **10**, 076116 (2025).

[20] D. A. B. Miller, C. Roques-Carmes, C. G. Valdez, A. R. Kroo, M. Vlk, S. Fan, and O. Solgaard, Universal programmable and self-configuring optical filter, *Optica* **12**, 1417 (2025).

[21] Y. Shen, N. C. Harris, S. Skirlo, M. Prabhu, T. Baehr-Jones, M. Hochberg, X. Sun, S. Zhao, H. Larochelle, D. Englund, and M. Soljačić, Deep learning with coherent nanophotonic circuits, *Nat. Photon.* **11**, 441 (2017).

[22] W. Bogaerts, D. Pérez, J. Capmany, D. A. B. Miller, J. Poon, D. Englund, F. Morichetti, and A. Melloni, Programmable photonic circuits, *Nature* **586**, 207–216 (2020).

[23] J. Capmany and D. Pérez, *Programmable Integrated Photonics* (Oxford Univ. Press, Oxford, 2020).

[24] F. Ashtiani, A. J. Geers, and F. Aflatouni, An on-chip photonic deep neural network for image classification, *Nature* **606**, 501 (2022).

[25] M. Reck, A. Zeilinger, H. J. Bernstein, and P. Bertani, Experimental realization of any discrete unitary operator, *Phys. Rev. Lett.* **73**, 58 (1994).

[26] D. A. B. Miller, Setting up meshes of interferometers – reversed local light interference method, *Opt. Express* **25**, 29233 (2017).

[27] B. E. A. Saleh, *Quantum Photonics: Bimodes, Qubits, and Biphotos* (Springer, 2025).

[28] M. Harling, V. A. Kelkar, K. C. Toussaint, and A. F. Abouraddy, Isoentropic partially coherent optical fields that cannot be interconverted unitarily, *Phys. Rev. A* **110**, 013505 (2024).

[29] L. Waller, G. Situ, and J. W. Fleischer, Phase-space mea-

surement and coherence synthesis of optical beams, *Nat. Photon.* **6**, 474 (2012).

[30] C. Okoro, H. E. Kondakci, A. F. Abouraddy, and K. C. Toussaint, Demonstration of an optical-coherence converter, *Optica* **4**, 1052 (2017).

[31] M. Harling, V. A. Kelkar, K. C. Toussaint, and A. F. Abouraddy, Locked entropy in partially coherent optical fields, *Phys. Rev. A* **109**, L021501 (2024).

[32] H. Gamo, Matrix treatment of partial coherence, *Prog. Opt.* **3**, 187 (1964).

[33] F. Gori, M. Santarsiero, and R. Borghi, Vector mode analysis of a Young interferometer, *Opt. Lett.* **31**, 858 (2006).

[34] A. F. Abouraddy, What is the maximum attainable visibility by a partially coherent electromagnetic field in Young's double-slit interference?, *Opt. Express* **25**, 18320 (2017).

[35] K. H. Kagalwala, G. Di Giuseppe, A. F. Abouraddy, and B. E. A. Saleh, Bell's measure in classical optical coherence, *Nat. Photon.* **7**, 72 (2013).

[36] M. Źukowski, A. Zeilinger, and M. A. Horne, Realizable higher-dimensional two-particle entanglements via multiport beam splitters, *Phys. Rev. A* **55**, 2564 (1997).

[37] A. Hashemi, A. Shiri, B. E. A. Saleh, A. Blanco-Redondo, and A. F. Abouraddy, Programmable on-chip synthesis and reconstruction of partially coherent two-mode optical fields, *arXiv:2601.09802* (2026).

[38] L. D. Faddeev, Algebraic aspects of Bethe ansatz, *Int. J. Mod. Phys. A* **10**, 1845 (1995).

[39] A. F. Abouraddy, K. H. Kagalwala, and B. E. A. Saleh, Two-point optical coherency matrix tomography, *Opt. Lett.* **39**, 2411 (2014).

[40] K. H. Kagalwala, H. E. Kondakci, A. F. Abouraddy, and B. E. A. Saleh, Optical coherency matrix tomography, *Sci. Rep.* **5**, 15333 (2015).

[41] D. F. V. James, P. G. Kwiat, W. J. Munro, and A. G. White, Measurement of qubits, *Phys. Rev. A* **64**, 052312 (2001).

[42] A. F. Abouraddy, A. V. Sergienko, B. E. A. Saleh, and M. C. Teich, Quantum entanglement and the two-photon stokes parameters, *Opt. Commun.* **210**, 93 (2002).

[43] R. Jozsa, Fidelity for mixed quantum states, *J. Mod. Opt.* **41**, 2315 (1994).

[44] C. Brosseau and A. Dogariu, Symmetry properties and polarization descriptors for an arbitrary electromagnetic wavefield, *Prog. Opt.* **49**, 315 (2006).

[45] S. Pai, B. Bartlett, O. Solgaard, and D. A. B. Miller, Matrix optimization on universal unitary photonic devices, *Phys. Rev. Appl.* **11**, 064044 (2019).

[46] B. A. Bell and I. A. Walmsley, Further compactifying linear optical unitaries, *APL Photon.* **6**, 070804 (2021).

[47] D. Griffiths, *Introduction to Elementary Particles* (Wiley-VCH, Weinheim, 2008).

[48] C. Roques-Carmes, S. Fan, and D. Miller, Measuring, processing, and generating partially coherent light with self-configuring optics, *Light Sci. Appl.* **13**, 260 (2024).

[49] P. Sanjari and F. Aflatouni, An integrated photonic-assisted phased array transmitter for direct fiber to mm-wave links, *Nat. Commun.* **14**, 1414 (2023).

[50] M. Harling, V. Kelkar, C. Okoro, M. Diouf, A. F. Abouraddy, and K. C. Toussaint, Reversible inter-degree-of-freedom optical-coherence conversion via entropy swapping, *Opt. Express* **30**, 29584 (2022).

[51] B. Wacogne and D. A. Jackson, Enhanced security in a coherence modulation system using optical path difference corruption, *IEEE Photon. Technol. Lett.* **8**, 947 (1996).

[52] W. T. Rhodes, A. Boughanmi, and Y. T. Moreno, High-security communication by coherence modulation at the photon-counting level, *Appl. Opt.* **55**, 3952 (2016).

[53] E. Baleine and A. Dogariu, Variable coherence tomography, *Opt. Lett.* **29**, 1233 (2004).

[54] D. Peng, Z. Huang, Y. Liu, Y. Chen, F. Wang, S. A. Ponomarenko, and Y. Cai, Optical coherence encryption with structured random light, *PhotonX* **2**, 6 (2021).

[55] X. Liu, X. Li, S. A. Ponomarenko, F. Wang, X. Peng, Y. Cai, and C. Liang, Unlocking secure optical multiplexing with spatially incoherent light, *Laser Photon. Rev.* **19**, 2401534 (2025).